MICROSTRUCTURES AND DEFORMATION MICROMECHANISMS IN DEFORMED BUNDLE OF FIBRES

P. Latil[1], L. Orgéas[1*], C. Geindreau[1], S. Rolland du Roscoat[1], P.J.J. Dumont[2], S. Le Corre[3]

[1]*CNRS / Université de Grenoble, Laboratoire Sols-Solides-Structures-Risques (3SR), BP53, 38041 Grenoble cedex 9, France*
[2]*CNRS / Institut Polytechnique de Grenoble, Laboratoire de Génie des procédés Papetiers (LGP2), BP65, 38402 Saint-Martin d'Hères cedex, France*
[3]*CNRS / Polytech'Nantes, Laboratoire de Thermocinétique de Nantes (LTN), BP50609, 44306 Nantes cedex 3, France*
**laurent.orgeas@3sr-grenoble.fr*

Keywords: fibre bundle, X-Ray microtomography, In situ compression, Micromechanics

Abstract
Two bundles of quasi-aligned elastic fibres were subjected to simple and plane strain compressions coupled with 3D in situ observations by using synchrotron X-Ray microtomography. First, at the bundle scale, due to the slight fibre misalignment allowed during simple compression, it is found that the consolidation is less marked and requires higher stress than during plane strain compression. For both loadings, the stress level and the external work undergo sharp hardening with fibre content. Second, using homemade procedures at the microscale, 3D images allow to follow each fiber centreline and so to identify relevant microstructural descriptors and deformation micromechanisms. Therewith, it is found that the elastic bending energy of fibres recorded during tests are much lower than the elastic energy associated with fibre-fibre contacts.

1 Introduction

Many fibrous reinforcements used in polymer composites are made up of continuous or discontinuous fibre bundles that undergo severe compression, shear and/or bending deformations during composite forming processes. Such meso-scale deformations induce complex micro-mechanisms at the fibre scale: important displacements and deformations such as, for instance, fibre orientation, stretching, bending, twisting, and creation/lost of fibre-fibre contacts [1-4]. These fibre scale mechanisms are complex and still not well understood. They greatly affect the rheological behaviour of the composites during processing; *e.g.* by modifying the permeability and the anisotropy of the fibrous reinforcements, and the final physical and mechanical properties of produced parts.
To better understand them, by using 3D imaging of micromechanical tests performed with fibre bundles, this study provides original experimental data concerning the 3D evolution of the fibrous microstructure and the deformation micromechanisms.

2 Materials and testing methods

Two compressions, *i.e.* a simple compression and a plane strain compression (SC and PS) were achieved with a model saturated fibre bundles made up of fluorocarbon fibres (cut from a fishing wire, $N \approx 330$ fibres of diameter $D = 0.16$ mm, length $L \approx 10$ mm, Young's modulus

E = 2 GPa, Poisson's coefficient ν = 0.3) impregnated with olive oil (viscosity μ = 70 mPa s). The fibre bundle compressions were carried out using an especially designed micro-rheometrer mounted on the ID19 beam line of the European Synchrotron Radiation Facility (ESRF). 3D images (voxel size of 7.5^3 µm^3) of the evolving fibrous microstructure were then obtained during the compression experiments by performing "Fast X-ray microtomography" (scanning times below 2 minutes) [5].

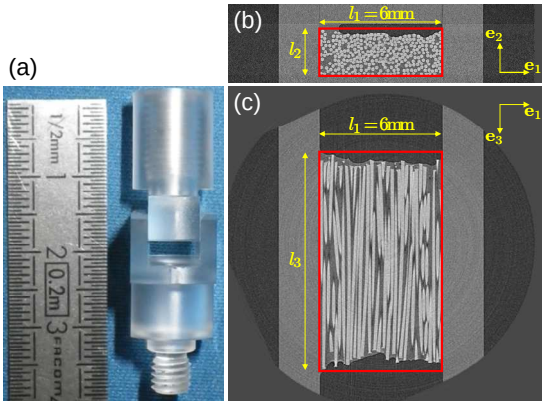

Figure 1. (a) Picture of the plane strain compression apparatus (width 6 mm). Reconstructed tomographic slices of the fibre bundle within the apparatus: (b) vertical and (c) horizontal cross sections.

After denoising and standard thresholding operations, the evolving fibrous phase was obtained as shown in figure 3 (a-d). We could then: (i) measure the fibre volume fraction ϕ, (ii) identify the fibre centerlines [5]. Then using fibre centerlines, the following measures could be achieved [5]:

- Determination of each fibre direction vector $\mathbf{p}^i$, expressed as the direction of the lower fibre inertia axis. From these vectors, the second order orientation tensor of fibres **A** [6] could be then be estimated.
- A local Frenet frame was assigned along curvilinear abscissa s of each centreline. Thereafter, a local centreline curvature $\kappa(s)$ was determined.
- The total number of fibre-fibre contacts N_c together with fibre-fibre contact direction vectors $\mathbf{q}^j$ were then measured. The second order orientation tensor of contacts **B** could be estimated. The average coordination number $\bar{z} = 2N_c / N$, N being the number of fibre within the bundle, was also estimated.
- The distance between two fibres in contact d^j was also calculated. Thereby, the indentation α^j of a contact j was estimated as: $\alpha^j = D - d^j$.

2 Results

2.1 At the meso-scale

At the meso-scale, *i.e.* the scale of the fibre bundle, the deformations in each direction can be calculated using 3D images: $\boldsymbol{\varepsilon} = \varepsilon_{11}\mathbf{e}_1 \otimes \mathbf{e}_1 + \varepsilon_{22}\mathbf{e}_2 \otimes \mathbf{e}_2 + \varepsilon_{33}\mathbf{e}_3 \otimes \mathbf{e}_3$ with $\varepsilon_{ii} = \ln(l_i/l_{i0})$ (see Fig. 1), together with its associated volume change ε_v and deviatoric strain ε_d defined in a similar manner as in [5]. It is shown that:

- The bundles were subjected to a high consolidation (see Fig. 2 (a-b)). The fibre volume fraction ϕ increases from about 40% to 55% for SC and from 45 to 75% for PS (see Fig. 2 (a)). This was accompanied with a large increase of the mean Cauchy stress tensor $\Sigma_{22} = F_2/(l_1 l_3)$ (F_2 being the compression force). Figure 2 (a) shows that

Σ_{22} is higher during SC than during PS. It was found that $\Sigma_{22} = k(\phi^n - \phi_0^n)$ were $n = 20$ for SC and 16 for PS. These high values are consistent with those reported in [2].

- SC exhibited a deviatoric deformation path $\varepsilon_d \propto -4\varepsilon_v$ while PS followed an œdometric deformation path where $\varepsilon_d = -\sqrt{3}/2\,\varepsilon_v$ (see Fig. 2 (c)).

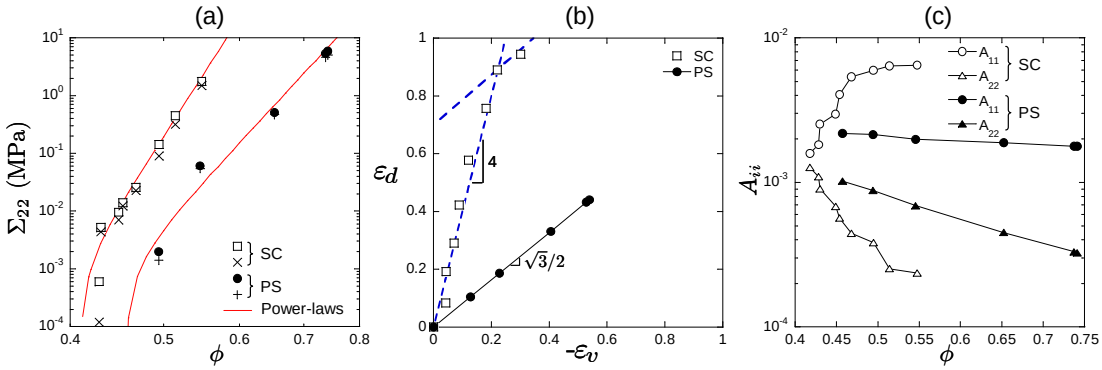

Figure 2. Mechanical response at the meso-scale. (a) Log-log graph of Σ_{22} *vs* fibre volume fraction ϕ (solid symbols represent peak stress and open symbols relaxed stress). (b) Deviatoric strain ε_d *vs* volumetric strain ε_v. (c) Evolution of fibre orientation during compression: A_{11} and A_{22} *vs* ϕ.

2.2 At the micro-scale

The skeletonisation of the fibre bundles, *i.e.* the identification of centerlines $\mathbf{x}^i$ of each of their fibres *i*, provides relevant microstructural and micromechanical information [5]:

- The orientation unit spheres [5,7,8] (where vectors $\mathbf{p}^i$ are in blue) and the associated orientation tensor **A** plotted in Figs. 3 (a-d) and Fig. 2 (g) shows that during compression, (i) the fibres remain mainly orientated in the $\mathbf{e}_3$-direction, (ii) the misalignment with respect to the $\mathbf{e}_2$-direction (the compression direction) strongly decreased for SC and PS while the misalignment in the $\mathbf{e}_1$-direction increased for SC and was stable for PS. This could explain the higher stress required to deform fibre bundle in SC (see Fig. 2(a)).

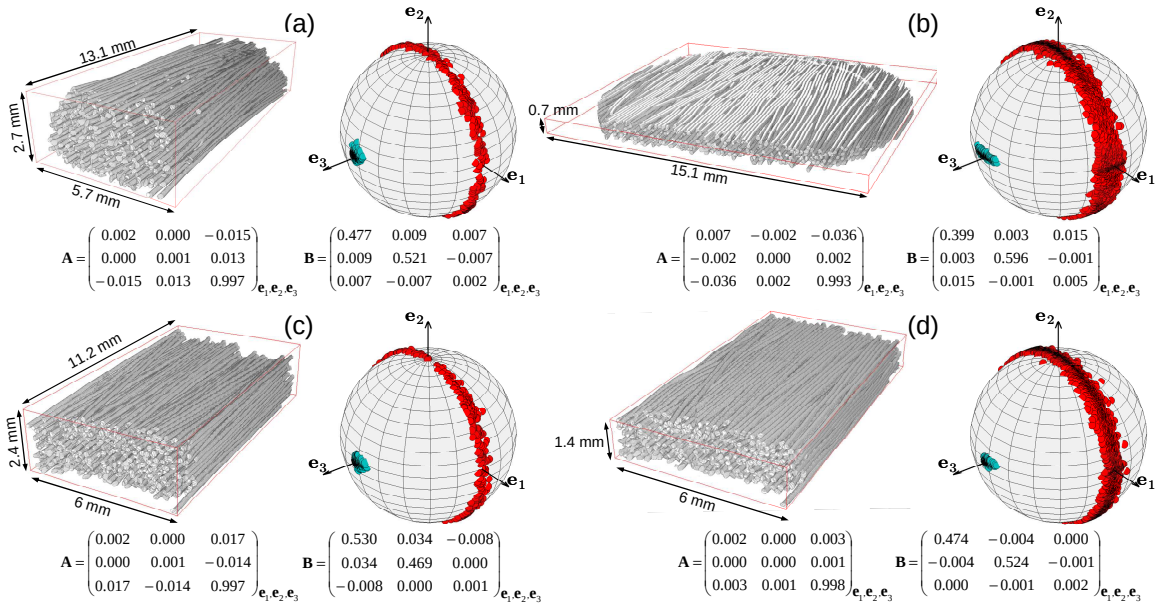

Figure 3. Microstructure at the micro-scale. Volume rendering of fibre bundles in the initial (a) and (c), and final states (b) and (d), for simple compression (a) and (b), and for plane strain compression (c) and (d).

- Fig. 4 (a) shows that the mean curvature $\overline{\kappa}$ was finite in the initial (undeformed) state with a corresponding average radius of curvature $\overline{R}^0 = 1/\overline{\kappa}^0 \approx 100\,\text{mm}$ (induced by the winding of fibres onto a reel). As revealed from this figure the curvatures $\overline{\kappa}$ increased importantly during compression and reached an average corresponding radius of curvature $\overline{R} = 1/\overline{\kappa} \approx 15$ mm.

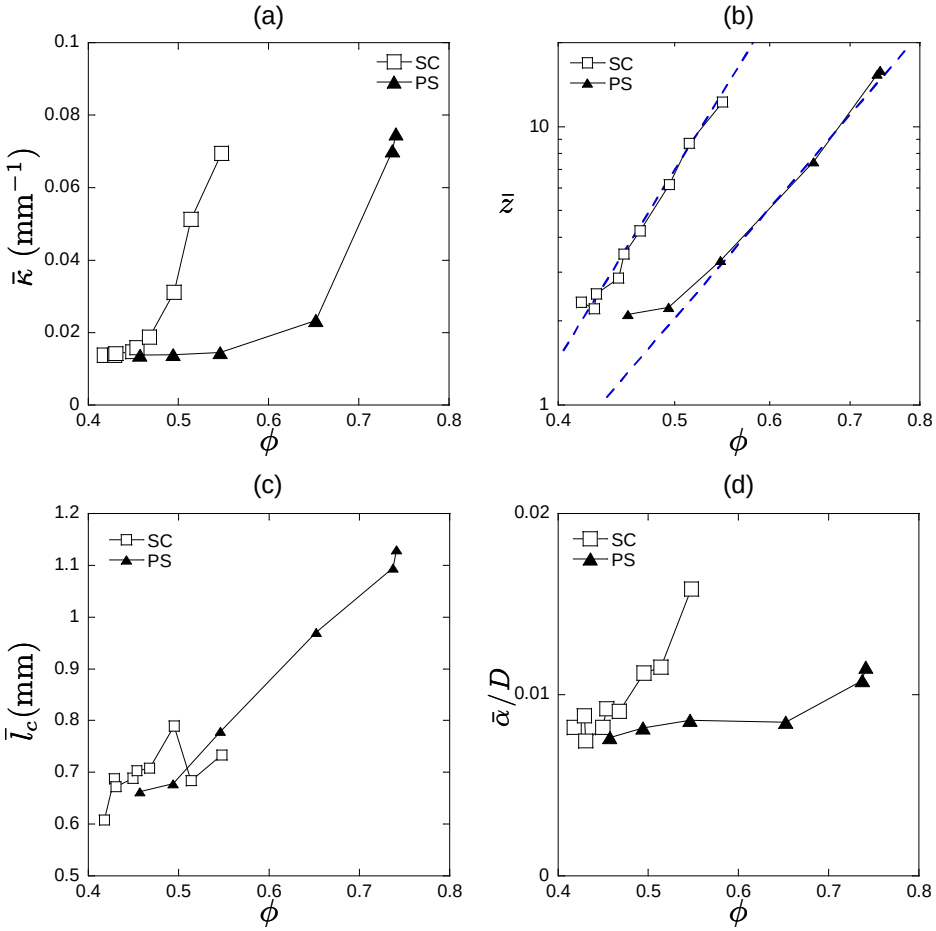

Figure 4. Microscopic parameters. (a) Mean curvature $\overline{\kappa}$ *vs* ϕ. (b) Mean coordination number $\overline{z}$ *vs* ϕ. (c) Mean length of contacts $\overline{l_c}$ *vs* ϕ. (d) Mean dimensionless indentation of contact $\overline{\alpha}/D$ *vs* ϕ.

- The orientation unit spheres [5,7,8] (where contacts appear in red) and the associated orientation tensor **B** plotted in Figs. 3 (a-d) show that contacts are mainly orientated in the compression direction $\mathbf{e}_2$. It also appears that the contact misalignment is more pronounced in the $\mathbf{e}_1$-direction for SC (following the fibre misalignment).
  Fig. 4 (b) shows the log-log evolution of $\overline{z}$ with respect to ϕ. $\overline{z}$ strongly increases from about 2 to 11 in the considered microstructures. Fig. 4 (b) also shows that the slope of the SC curve is higher than that of the PS. This should partially explain the difference of power law exponent *n* highlighted in previous section (Fig. 2(a)). Fig. 4 (c) shows that the mean contact length $\overline{l_c}$ increases during compression of fibre bundle. Fig. 4 (d) shows that the mean contact indentation $\overline{\alpha}$ also increases during compression. These two additional phenomena also contribute to the increase of the consolidation stress Σ_{22}.

3 Discussion

From the evolution of the microstructure descriptors shown in the previous section, it is possible to reveal the deformation micromechanisms involved during the compression and to quantify their relative importance.

- The overall elastic bending energy W_{bend} is expressed as:

$$W_{bend} = \sum_{i=1}^{N} W_b^i, \quad \text{where} \quad W_b^i = \frac{1}{2}\int_0^{L^i} EI\left(\kappa^i(s) - \bar{\kappa}^0\right)^2 \mathrm{d}s, \tag{1}$$

where W_b^i is the elastic bending energy of fibre i (current and initial curvatures $\bar{\kappa}$ and $\bar{\kappa}^0$). $I = \pi D^4/64$ is the quadratic moment of the circular cross section of fibres.

- The overall elastic energy associated to contacts W_{cont} is estimated as:

$$W_{cont} = \sum_{j=1}^{N_c} W_c^j, \quad \text{where} \quad W_c^j = \int_0^{l_c^j} \overline{W_c^j}(s)\,\mathrm{d}s \tag{2}$$

is the elastic contact energy contact. The elastic contact energy per unit length $\overline{W_c^j}(s)$ was calculated as follows:

$$\overline{W_c^j}(s) = \int_0^{\alpha(s)} \overline{P^j}(s)\,\mathrm{d}\alpha, \tag{3}$$

In order to estimate the contact force per unit length $\bar{P}$, the Jonhson model for parallel cylinder in contact [9] was used:

$$\bar{P}^j(s) \approx K\alpha^j(s)^{20/17} \tag{5}$$

K is an elastic coefficient calculated using elastic properties of the fibre and the Jonhson model [9]. Fig. 5 shows the evolution of W_{bend} and W_{cont} with the fibre content ϕ. This figure first shows that the energy associated to fibre bending is one decade lower than the contact associated energy. Furthermore, W_{cont} is very close to the external work W_{ext} required to deform the bundles. This also shows that for the considered meso-scale loadings, fibre-fibre contacts mainly govern the mechanical behaviour of the fibre bundles.

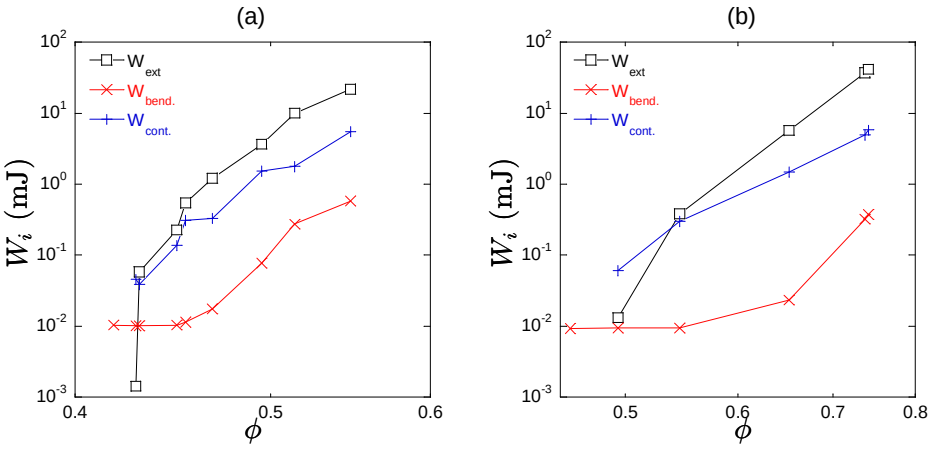

Figure 5. Elastic deformation energies. (a) Simple compression and (b) plane strain compression tests.

4 Conclusion

Based on 3D images obtained by X-ray microtomography, we have proposed microstructural and micromechanical measurements of the deformation of fibre bundles achieved during two compression tests. These new experimental data allow a better understanding of their deformation micro-mechanisms. Thus, it was found that (i) the deformation path in compression (CS *vs* PS) greatly influences the mechanical response of the fibre bundle, (ii) the main deformation micro-mechanism involved in fibre bundle deformation is mainly governed by fibre-fibre contacts through the coordination number, the contact geometries and the fibre deformations in the contact zones. These aspects will be relevant to provide physics based models for the fibre bundle behaviours and to improve composite forming simulation.

References

[1] Robitaille F, Gauvin R, Compaction of textile reinforcements for composites manufacturing. i: Review of experimental results, *Polym Compos*, **19**, pp. 198–216 (1998).
[2] Toll S., Packing mechanics of fiber reinforcements, *Polym Eng Sci*, **38**, pp 1337–50 (1998).
[3] Badel P, Vidal-Salle E, Maire E, Boisse P. Simulation and tomography analysis of textile composite reinforcement deformation at the mesoscopic scale, *Compos Sci Technol*, **68**, pp 2433–40 (2008).
[4] Le TH, Dumont P, Orgéas L, Favier D, Salvo L, Boller E. X-ray phase contrast microtomography for the analysis of the fibrous microstructure of SMC composites, *Compos Part A*, **39**, pp 91–103 (2008).
[5] Latil P, Orgéas L, Geindreau C, Dumont PJJ, Rolland du Roscoat S. Towards the 3D in situ characterisation of deformation micro-mechanisms within a compressed bundle of fibres, *Compos Sci Technol*, **71**, pp 480–8 (2011).
[6] Advani SG, Tucker CL. The use of tensors to describe and predict fiber orientation in short fiber composites. *J Rheol*, **3**(8), pp 751–84 (1987).
[7] Orgéas L, Dumont PJJ, Vassal J-P, Guiraud O, Michaud V, Favier D. In-plane conduction of polymer composite plates reinforced with architectured networks of Copper fibres, J Mater Sci, **47**, pp 2932–42 (2012).
[8] Guiraud O, Orgéas L, Dumont PJJ, Rolland du Roscoat S, Microstructure and deformation micromechanisms of concentrated fiber bundle suspensions: An analysis combining x-ray microtomography and pull-out tests, *J Rheol*, **56**(3), 593-623 (2012).
[9] Johnson, K., Contact Mechanics, *Cambridge University Press* (1985).